Journal of Power Sources 232 (2013) 279–285

Contents lists available at SciVerse ScienceDirect

Journal of Power Sources

journal homepage: www.elsevier.com/locate/jpowsour

Thermal and electrochemical properties of $PrBa_{0.5}Sr_{0.5}Co_{2-x}Fe_xO_{5+\delta}$ ($x = 0.5, 1.0, 1.5$) cathode materials for solid-oxide fuel cells

Long Jiang [a,b], Tao Wei [a], Rui Zeng [a], Wu-Xing Zhang [a], Yun-Hui Huang [a,*]

[a] State Key Laboratory of Material Processing and Die and Mould Technology, School of Materials Science and Engineering, Huazhong University of Science and Technology, Wuhan, Hubei 430074, China

[b] School of Physical Science and Technology, Yangtze University, Jingzhou, Hubei 434023, China

HIGHLIGHTS

- ► Layered perovskite $PrBa_{0.5}Sr_{0.5}Co_{2-x}Fe_xO_{5+\delta}$ (PBSCF) was investigated as cathode materials for solid oxide fuel cells.
- ► Partial substitution of Fe for Co can effectively decrease thermal expansion coefficient to match the electrolyte.
- ► PBSCF with $x = 0.5$ shows the highest power density.
- ► Microstructure, conductivity and polarization resistance play important roles in electrochemical performance.

ARTICLE INFO

Article history:
Received 22 August 2012
Received in revised form
12 December 2012
Accepted 14 January 2013
Available online 18 January 2013

Keywords:
Solid-oxide fuel cell
Perovskite
Cathode
Electrochemical performance

ABSTRACT

Layered perovskite $PrBa_{0.5}Sr_{0.5}Co_{2-x}Fe_xO_{5+\delta}$ (PBSCF, $x = 0.5, 1.0, 1.5$) oxides are designed and evaluated as cathode materials for solid-oxide fuel cells. Effect of Fe/Co molar ratio on structural, thermal and electrochemical properties for PBSCF is systematically investigated. With increasing x from 0.5 to 1.5, the structure does not change but the lattice parameters increase. At the same time, thermal expansion coefficient decreases, which is helpful to thermally match with the electrolyte. From X-ray photoelectron spectra, it can be seen that both Fe and Co exist in a mixed oxidation state. Fe ions are prone to high oxidation state (Fe^{3+} and Fe^{4+}), while Co ions basically exhibit low oxidation state (Co^{2+} and Co^{3+}). The PBSCF samples exhibit a semiconductor–metal transition in the temperature range of 250–300 °C. With increasing Fe substitution content for Co, the electrode polarization resistance increases. The PBSCF ($x = 0.5$) cathode exhibits the highest power density of 697 mW cm^{-2} at 850 °C. The cell power output strongly depends on microstructure, electronic conductivity and electrochemical resistance.

© 2013 Elsevier B.V. All rights reserved.

1. Introduction

Solid-oxide fuel cells (SOFCs) have long been investigated as energy conversion devices with high efficiency, low pollution emission and extensive fuel flexibility [1,2]. Traditional SOFCs that are operated at high temperature around 1000 °C encounter a series of problems, such as materials aging, thermal expansion mismatch and high fabrication cost. Recently, great effort has been devoted to lowering the operation temperature down to the intermediate range of 500–800 °C, which can not only extend the choice range of SOFC materials, but also reduce the cost of practical application. However, lowering operation temperature obviously leads to loss of power density due to electrolyte ohmic resistance and electrode polarization, and decrease of the electrode catalytic activity for oxygen reduction reaction. Conventional $(La,Sr)MnO_3$ (LSM) based cathode materials have high electronic conductivity and chemical stability at high temperature, but their oxide-ion conductivity and electronic conductivity below 700 °C are poor [3].

In recent years, mixed ionic-electronic conductors (MIECs) with layered perovskite structure such as $LnBaCo_2O_{5+\delta}$ (Ln = Y, Pr, Nd, Sm, Gd) have received widespread attention [4–6]. $LnBaCo_2O_{5+\delta}$ show a cation-ordered double perovskite structure with alternating Ln–O and Ba–O layers [7]. In this structure, the oxygen vacancies mainly distribute in the LnO_δ layers [8], which can greatly enhance the diffusivity of oxide ions in the bulk of the material and possibly supply surface defect sites with enhanced reactivity toward molecular oxygen. These characteristics are helpful to improve the electrochemical performance of the cathode.

Among $LnBaCo_2O_{5+\delta}$ oxides, $PrBaCo_2O_{5+\delta}$ has been attracted tremendous interest due to high electronic conductivity, low

* Corresponding author. Tel.: +86 27 87558237.
E-mail addresses: huangyh@mail.hust.edu.cn, yunhuihuang@yahoo.com (Y.-H. Huang).

0378-7753/$ – see front matter © 2013 Elsevier B.V. All rights reserved.
http://dx.doi.org/10.1016/j.jpowsour.2013.01.064

cathode polarization and excellent electrochemical performance [9–14]. Sr-doped oxide $PrBa_{0.5}Sr_{0.5}Co_2O_{5+\delta}$ shows improved cell performance especially at intermediate temperature [15,16]. Unfortunately, the cobalt-based double perovskites usually suffer from high thermal expansion coefficient (TEC) ($>20 \times 10^{-6}$ K^{-1}) [17], which results in mismatch with conventional electrolyte materials.

In this work, we used Fe ions to partially substitute Co ions in $PrBa_{0.5}Sr_{0.5}Co_2O_{5+\delta}$ to lower the TEC and improve the electrochemical performance. The oxides $PrBa_{0.5}Sr_{0.5}Co_{2-x}Fe_xO_{5+\delta}$ with $x = 0.5$, 1.0 and 1.5 were designed and focused on for SOFC cathode materials, which Fe/Co molar ratio is 1:3, 1:1 and 3:1, respectively. The dependence of Fe/Co molar ratio on structural, thermal and electrochemical properties has been systematically investigated.

2. Experimental

2.1. Materials preparation

$PrBa_{0.5}Sr_{0.5}Co_{2-x}Fe_xO_{5+\delta}$ (PBSCF) series samples ($x = 0.5$, 1.0 and 1.5, abbreviated as PBSCF05, PBSCF10 and PBSCF15, respectively) were prepared by a sol–gel method. Stoichiometric amounts of Pr_6O_{11} (99.9%), $Sr(NO_3)_2$ (99.5%), $Ba(NO_3)_2$ (99.5%), $Co(NO_3)_2 \cdot 6H_2O$ (99%), $Fe(NO_3)_3 \cdot 9H_2O$ (98.5%) were used as starting materials. Pr_6O_{11} was first dissolved completely in concentrated nitric acid; $Sr(NO_3)_2$, $Ba(NO_3)_2$, $Co(NO_3)_2 \cdot 6H_2O$ and $Fe(NO_3)_3 \cdot 9H_2O$ were dissolved into deionized water. Then the two solutions were mixed together, followed by adding a combined complexant solution of citric acid and ethylenediaminetetraacetic acid (EDTA). The molar ratio of total metal ions, EDTA and citric acid was 1:1:2. An appropriate amount of ammonia was added to adjust pH value of the solution to 7 ~ 8. The precursor solution was subsequently heated at 90 °C under stirring to form a viscous gel, and then the gel was baked at 150 °C overnight. The gel was calcined at 400 °C for 6 h to achieve a powder. The powder was ground and finally sintered at 1000 °C for 10 h.

$La_{0.8}Sr_{0.2}Ga_{0.83}Mg_{0.17}O_{2.815}$ (LSGM) and $Ce_{0.8}Sm_{0.2}O_{1.9}$ (SDC) were synthesized via solid state reaction, as described in detail elsewhere [18,19]. The anode was the mixture of NiO and SDC power with a weight ratio of 65:35.

2.2. Characterizations

The phase of the samples was characterized with X-ray diffraction (XRD) by using the Philips X'Pert PRO diffractometer operating with CuKα radiation. A scanning electron microscope (SEM) was used to inspect the morphology of the samples. Surface analysis was performed on an X-ray photoelectron spectrometer (XPS, MULT1LAB2000, VG). The electronic conductivity was measured on an RTS-8 digital instrument in stagnant air with a standard four-probe method. For the conductivity measurement, the sample was pressed into a pellet with diameter of 13 mm and thickness of 1 mm under a pressure of 100 MPa followed by sintering at 1000 °C for 10 h; Ag wires and Ag paste were used as current collector. Thermal expansion coefficients (TECs) were measured on the rectangular-shaped bar samples (5 mm × 5 mm × 20 mm) from room temperature to 900 °C at a heating rate of 5 °C min^{-1} by using a dilatometer (NETZSCH STA449c/3/G). Thermogravimetric (TG) behaviors were checked by a Stanton STA 781 instrument.

The single fuel cells were fabricated using electrolyte-supported technique to form construction of NiO + SDC/SDC/LSGM/PBSCF. 300 μm thick LSGM served as the electrolyte. The buffer layer SDC was uniformly screen-printed onto one side of the LSGM disk, followed by being fired at 1300 °C in air for 1 h. The anode ink (NiO + SDC) was subsequently printed on the buffer layer and fired at 1250 °C in air for 2 h. The cathode slurry was screen-printed onto the other side of LSGM disk and sintered 950 °C for 2 h to form a thin film (area 4 mm × 5 mm). The cells were tested from 700 to 850 °C with hydrogen (flow rate 50 mL min^{-1}) as fuel and the static air as oxidant.

Electrochemical impedance spectra (EIS) and power output measurements of the cells were performed on the PARSTAT2273 electrochemical system. The impedance was detected over a frequency range from 10 mHz to 100 kHz with 10 mV ac signal amplitude under open circuit voltage. The EIS fitting analysis was controlled with the program Zview from EChem Software.

3. Results and discussion

3.1. Crystal structure

The XRD patterns are presented in Fig. 1a for the PBSCF samples obtained by sintering at 1000 °C for 10 h. All PBSCF05, PBSCF10 and PBSCF15 possess orthorhombic lattice geometry with space group Pmmm; no impurity phase appears. It indicates that partial substitution of Fe for Co does not affect the formation of layered perovskite phase. It should be pointed out that for the similar oxide $NdBaCo_{2-x}Fe_xO_{5+\delta}$, the structure changes from tetragonal (space group: P4/mmm) to cubic (space group: Pm-3m) with increasing Fe doping level x from 0.5 to 1.0 [20]. The different structure variation in our case is due to the cationic radii and the introduction of Sr^{2+} ions. With increasing Fe content x, the main diffraction peaks obviously shift to lower 2θ (Fig. 1b), indicative of expansion of the perovskite lattice. The lattice parameters calculated by the Jade software are listed in Table 1. As x increases, all of the lattice parameters a, b, c and V increase. In PBSCF, the lattice expansion is ascribed to two factors: one is the substitution of Fe ions with larger radius for Co ions, and the other is the cationic valence change due to the substitution.

3.2. XPS analysis

The XPS spectra were used to characterize the element chemical environment. The chemical environments of O, Fe and Co ions were estimated by curve-fitting of the O 1s, Fe 2p and Co 2p spectra, as shown in Fig. 2. In Fig. 2a, the O 1s core-level spectrum consists of two components at 528.5 and 531.2 eV. The former is a typical feature of hydroxyl group and carbonate structure (O_H), and the latter comes from the lattice O^{2-} (O_L) [21,22]. No obvious change in the O 1s profile with increasing Fe substitution level x. Falcon et al. [23] reported that the O 1s profile strongly depends on the alkaline-earth element at the A-site. In our case, since the A-site alkaline-earth component ($PrBa_{0.5}Sr_{0.5}$) keeps unchanged, it is difficult to

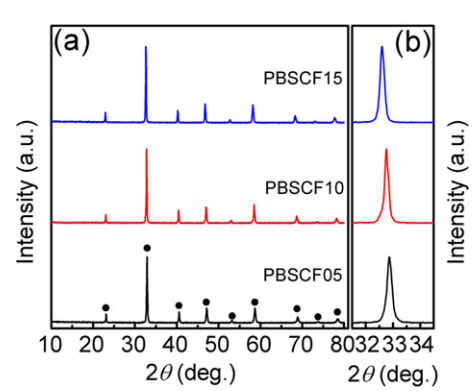

Fig. 1. XRD patterns of PBSCF samples after calcination at 1000 °C for 10 h.

Table 1
Lattice parameters obtained from Jade for the PBSCF samples.

Sample	Space group	Lattice parameter			Cell volume V (nm^3)
		a (nm)	b (nm)	c (nm)	
$x = 0.5$	Pmmm	0.3851(1)	0.3854(3)	0.7715(1)	0.1144(6)
$x = 1.0$	Pmmm	0.3865(7)	0.3864(2)	0.7727(6)	0.1154(8)
$x = 1.5$	Pmmm	0.3883(4)	0.3884(5)	0.7765(5)	0.1171(4)

distinguish the variation of O content from the XPS spectrum with changing the Fe/Co ratio at the B-site. Quantitative analysis of O content for each sample was carried out by iodometric titration method, as discussed later.

Fig. 2b shows the asymmetric Fe 2p core-level spectra of the PBSCF samples. Two different valences, Fe^{3+} and Fe^{4+}, appear in each sample. The doublet peaks with binding energy at 710.7 and 723.3 eV can be assigned to the Fe^{3+} $2p_{3/2}$ and $2p_{1/2}$ spectrum, respectively. Interestingly, a weak single peak at 715.8 eV appears between the above doublet peaks, corresponding to the Fe^{4+} $2p_{3/2}$. For the three samples with different Fe content, the XPS features are almost same. Fe^{3+} coexists with Fe^{4+} in these samples independent of the Fe content. Similar phenomenon was also observed by Jung et al. in perovskite oxide $Ba_{0.5}Sr_{0.5}Co_xFe_{1-x}O_{3-\delta}$ [24].

In Fig. 2c, the XPS spectra of Co 2p are also asymmetric. The main peaks located at 777.7 and 780.2 eV are obviously distinguishable from each other, representing Co^{2+} and Co^{3+}. The spectra with binding energy of 793.1 and 795.9 eV are satellite peaks of Co 2p, which is due to oxygen vacancies in the perovskite structure [25]. The mixture valence of Co^{3+} and Co^{2+} exists in these oxides. An additional weak peak located at binding energy of 784.5 eV is assigned to the Co^{4+} state. From the peak intensity of XPS spectra, we can judge that only a tiny of Co^{4+} ions exist in PBSCF.

From XPS, we can conclude that both Fe and Co exist in a mixed oxidation state. Fe ions are prone to high oxidation state (Fe^{3+} and Fe^{4+}), while Co ions basically exhibit low oxidation state (Co^{2+} and Co^{3+}). The valence remains unchanged with Fe substitution for Co in PBSCF, indicating that the occupancy sites of Fe and Co ions do not change with the Fe/Co ratio. At the same time, the XPS analysis further confirms that the lattice expansion is caused by the substitution of larger Fe ions for Co ions.

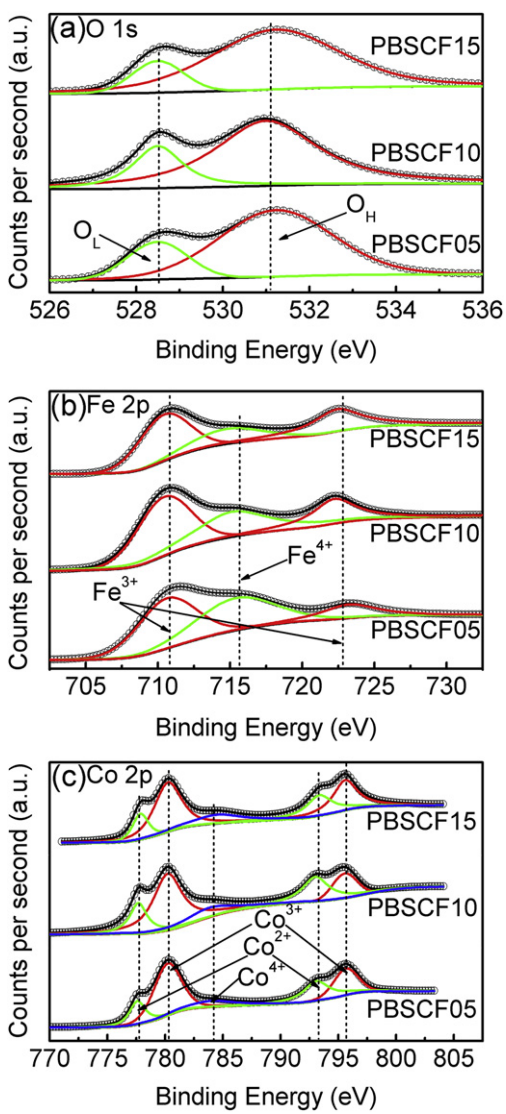

Fig. 2. XPS spectra at room temperature for the PBSCF samples: (a) O 1s, (b) Fe 2p, and (c) Co 2p.

3.3. Electrical conductivity

Fig. 3 shows conductivity (σ) of the PBSCF samples measured in air from room temperature to 850 °C. With increasing temperature, the conductivity for all samples increases and reaches the maximum in the range of 250–350 °C that corresponds to the metal–insulator transition temperature (T_{MI}). The PBSCF samples exhibit a typical semiconductor-like behavior, which can be ascribed to small polaron hopping conduction since the localized electronic carriers have a thermally activated mobility [26]. If temperature is higher than T_{MI}, the value of σ for all samples begins to decrease with increasing temperature, and the samples exhibit a metal-like behavior. This metal-like transport behavior is due to the orbital overlap between Co 3d and O 2p, which is the characteristic feature for the cobalt-based perovskite oxides [27]. Moreover, the σ decreases as the Fe substitution content x increases, which is similar to the recent report [28]. The value of σ for PBSCF is as high as 60–769 S cm^{-1} in the temperature range of 250–850 °C, much higher than that of $PrBaCo_{2-x}Fe_xO_{5+\delta}$. The enhanced conductivity can be attributed to the smaller lattice volume due to substitution of 50% Sr^{2+} for Ba^{2+} [29]. In addition, the T_{MI} for PBSCF depends on x; it increases with increasing x. The T_{MI} of conductivity in Fig. 3 should correspond to the loss of lattice oxygen [30]. Conder et al. [31] confirmed by using differential scanning calorimetry (DSC) method that the T_{MI} is related to the oxygen content in cobalt-based

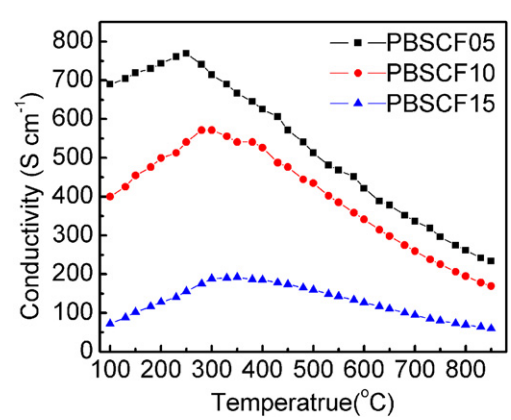

Fig. 3. Temperature dependence of electrical conductivity for the PBSCF samples in air.

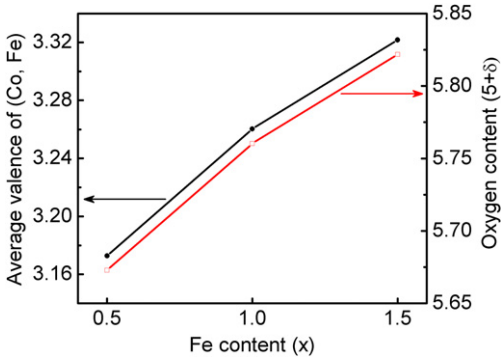

Fig. 4. Dependence of average valence of (Co, Fe) and oxygen content on Fe content in PBSCF.

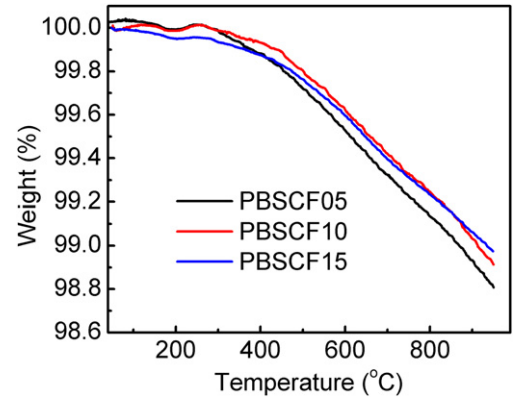

Fig. 5. TGA curves of the PBSCF samples in the temperature range of 40–950 °C in air.

double layered perovskite oxides, revealing that the oxygen content $(5 + \delta)$ in these samples increases with increasing substitution content of Fe for Co.

In order to determine the oxygen content $(5 + \delta)$ and average valence of (Co, Fe) in PBSCF, iodometric titration method was used. As described in detail elsewhere [18,32], the whole reactions can be expressed as follows:

$$2M^{3+} + 2I^- = I_2 + 2M^{2+} \ (M = Co,\ Fe) \quad (1)$$

$$2S_2O_3{}^{2-} + I_2 = 2I^- + S_4O_6{}^{2-} \quad (2)$$

Fig. 4 shows the dependence of average valence of (Co, Fe) and oxygen content on the Fe content x for PBSCF. The valence values are also listed in Table 2. We can see that the oxygen content increase with x. This can be explained by the stronger Fe–O band compared to the Co–O band [33]. A similar variation trend for the average valence of (Co, Fe) is also seen in Fig. 4. The higher the average valence of (Co, Fe) in these oxides, the more oxygen content $(5 + \delta)$ is needed to keep charge neutrality.

3.4. Thermogravimetry and thermal expansion behavior

Fig. 5 shows the TGA curves of the PBSCF samples during heating progress. The three samples exhibit similar thermal behavior. A slight weight loss before 200 °C is due to the evaporation of moisture. A significant linear weight loss from 250 °C should correspond to the removal of the lattice oxygen [34,35]. This part of loss is 1.20, 1.10 and 1.03% for PBSCF05, PBSCF10 and PBSCF15, respectively. Obviously, increasing Fe substitution gives rise to lower weight. Reduced oxygen removal from the lattice in the sample with high Fe content implies that the Fe–O bond is stronger than Co–O band in the lattice.

Fig. 6 shows the linear thermal expansion ($\Delta L/L_0$) and TECs from 40 °C to 900 °C for the PBSCF samples. From Fig. 6a, we can see that the $\Delta L/L_0$ is not exactly linearly dependent on temperature. An inflection occurs on the slope around 250 °C. In Fig. 6b, the variation of TEC clearly shows this inflection point at about 250 °C, which agrees well with the weight change in the TG curve. The inflection of TEC or $\Delta L/L_0$ could be related with the loss of lattice oxygen and the valence change of the transition metal (Co, Fe) ions. The average TEC values of the PBSCF samples at temperature range of 250–900 °C are listed in Table 2. The TEC value decreases from 21.3×10^{-6} K^{-1} to 19.2×10^{-6} K^{-1} with increasing Fe content from $x = 0.5$ to 1.5. Decreasing TEC is helpful for the PBSCF cathode to thermally match the LSGM electrolyte with TEC of (10–12.4) $\times 10^{-6}$ K^{-1}. The reduction in TEC with increasing Fe substitution may be ascribed to the expanded lattice. The substitution of larger Fe ions for Co leads to the lattice expansion. In addition, more oxygen content with increasing Fe content can provide more wide space to accommodate volume variation as temperature increases.

Table 2
Thermal expansion coefficients (TECs), average valence of (Co, Fe), oxygen content and resistances at 800 °C for the PBSCF samples.

Sample	TEC ($\times 10^{-6}$ K^{-1}) 250–900 °C	Average valence of (Co, Fe)	Oxygen content $(5 + \delta)$	Resistance (Ω cm^2) R_o	R_{tot}	R_p
$x = 0.5$	21.3	3.17	5.67	0.141	0.211	0.070
$x = 1.0$	20.9	3.26	5.76	0.143	0.220	0.077
$x = 1.5$	19.2	3.32	5.82	0.145	0.301	0.156

3.5. Microstructure and electrochemical performance

The SEM images of surface-view and cross-view for the PBSCF cathodes are shown in Fig. 7. From Fig. 7a–c, we can see that the PBSCF particles distribute uniformly and the mean particle size is less than 2 μm. The porous microstructure is clearly observed. From the cross section morphology in Fig. 7d–f, clear connection can be seen between the cathode and the electrolyte. The porosity in PBSCF provides sufficient triple phase boundary (TPB) for electrochemical reaction. The sufficient TPB is available to dominate charge transfer while the large particle surface favors surface adsorption and diffusion of oxygen [36]. For PBSCF05, the size distribution of particles is uniform, leading to a high porosity. With increasing x, the particle distribution becomes nonuniform and

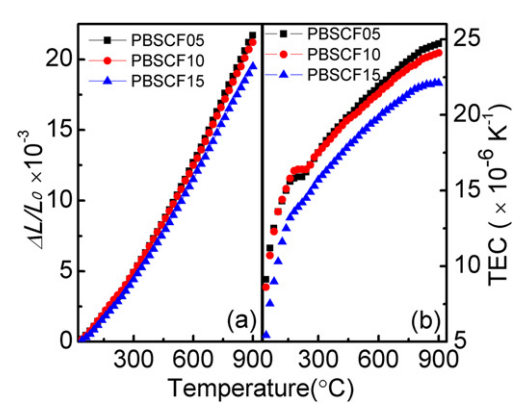

Fig. 6. (a) Thermal expansion ($\Delta L/L_0$) and (b) the corresponding TECs as functions of temperature for PBSCF measured in air from 40 °C to 900 °C.

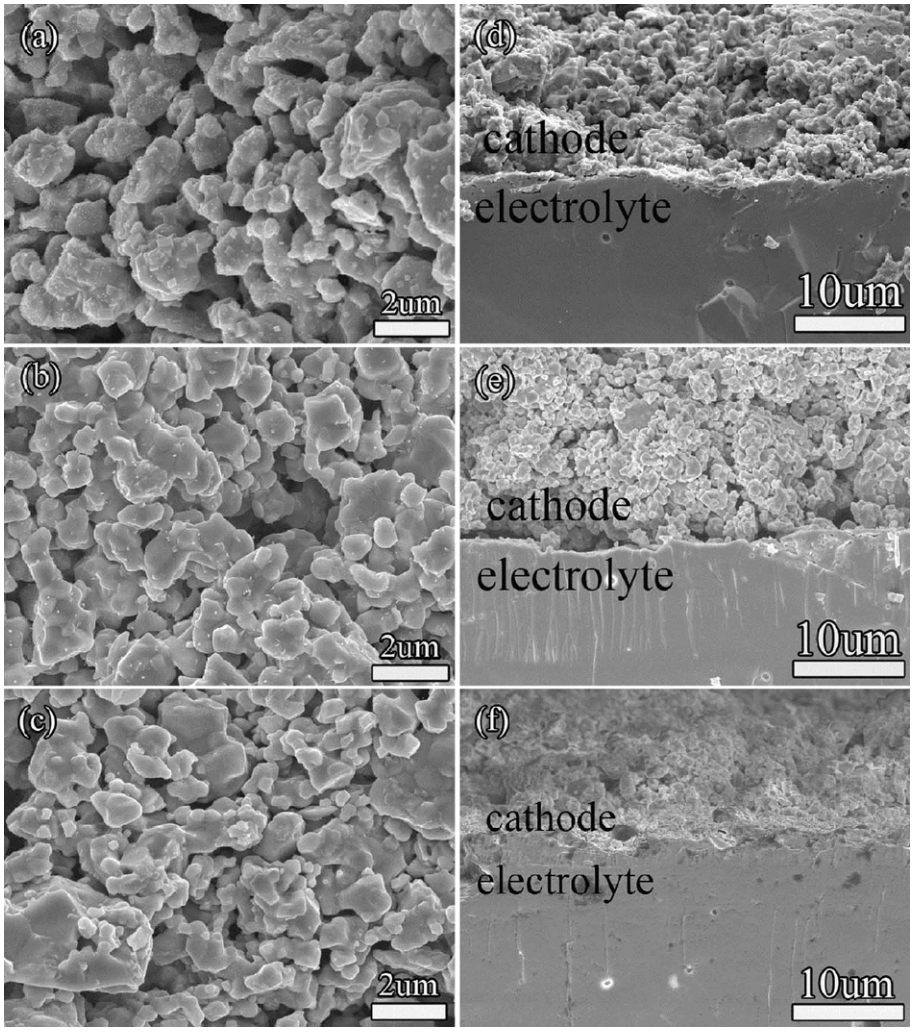

Fig. 7. SEM images of the surface-view and cross-view for the PBSCF cathodes: (a) and (d) PBSCF05; (b) and (e) PBSCF10; (c) and (f) for PBSCF15.

grain-agglomeration becomes more serious, the electrode microstructure becomes increasing dense, an obvious densification layer forms between PBSCF15 cathode and LSGM electrolyte from the fracture cross section, which not only reduce the length of TPB but also slow the surface oxygen diffusion. That means it is detrimental to the electrode with increase of Fe/Co ratio. To further check the chemical compatibility between the PBSCF electrode and the LSGM electrolyte, we mixed PBSCF and LSGM powers in a weight ratio of 1:1 and sintered at 950 °C for 2 h. Fig. 8 shows the XRD patterns of the mixture after heat treatment. No new phase was detected from XRD, indicating that no reaction occurs between PBSCF and LSGM. This demonstrates that the PBSCF cathode is chemically stable by connection with LSGM up to 950 °C.

The PBSCF samples were evaluated as cathode materials for SOFCs. Fig. 9 shows power density and cell voltage as functions of current density for the single cells with PBSCF as cathodes. Among the PBSCF cathodes, PBSCF05 shows the highest power density from 700 to 850 °C. For example, the maximum power density (P_{max}) at 850 °C reaches 697, 649 and 456 mW cm^{-2} for PBSCF05, PBSCF10 and PBSCF15, respectively. The decrease of P_{max} with increasing x is consistent well with the evolution of electronic conductivity in Fig. 3. For the typical PBSCF05, the P_{max} values are 590, 478 and 361 mW cm^{-2} at 800, 750 and 700 °C, respectively. This means that the PBSCF cathode material delivers remarkable power output at intermediate temperature.

We investigated the electrochemical stability of the PBSCF cathode materials. The single cells NiO + SDC/SDC/LSGM/PBSCF were operated at 800 °C for 10 h under a constant voltage loading of 0.6 V. The power densities of the cells are presented in Fig. 10. Although there is a little instability in the power output due to the testing disturbance, no obvious degradation is observed during the running process, indicating that the electrochemical performance

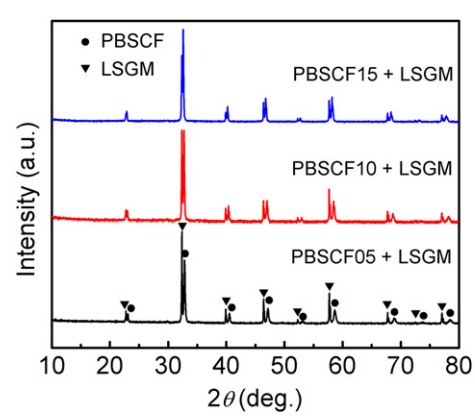

Fig. 8. XRD patterns for the mixtures of PBSCF and LSGM sintered at 950 °C for 2 h.

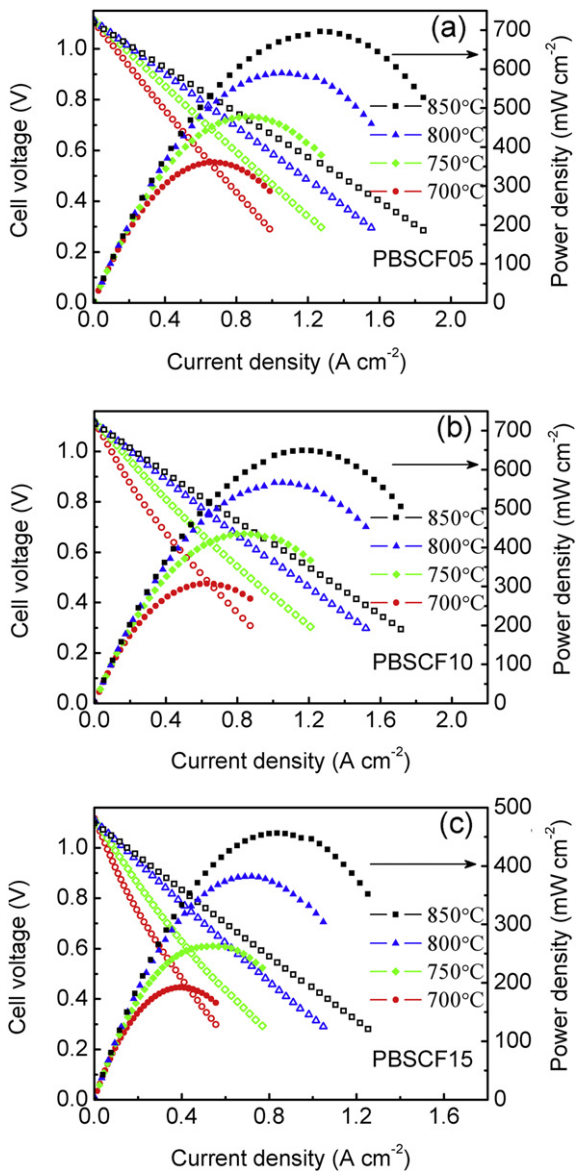

Fig. 9. Electrochemical performance of the single cells NiO–SDC/SDC/LSGM/PBSCF measured at 700–850 °C: (a) PBSCF05, (b) PBSCF10, and (c) PBSCF15.

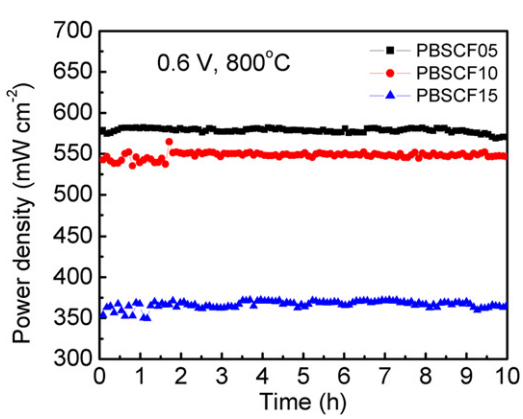

Fig. 10. Power density as a function of operation time at 800 °C under a loading voltage of 0.6 V for the cells with different PBSCF cathodes.

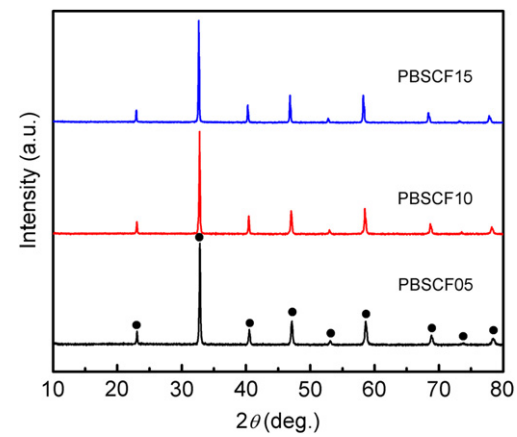

Fig. 11. XRD patterns for the PBSCF samples annealed at 800 °C for 100 h.

is basically stable for these cathodes. Among them, PBSCF05 still exhibits the highest power output. In order to further evaluate the structural stability, the materials were annealed at 800 °C for 100 h in air. The XRD patterns in Fig. 11 shows that no phase transition appears for all three samples, demonstrating that they can endure a long-term operation under the cathode atmosphere (air).

Electrochemical impedance was further measured to clarify the cell power output. Fig. 12 shows the impedance spectra of symmetric PBSCF cathodes on LSGM electrolyte measured at 800 °C in air. The impedance response can account for oxygen reduction reaction on the cathode. The intercept with the real axis at high frequency represents the ohm resistance (R_o) from the electrolyte and current collector, while the intercept with the real axis at low frequency represents the total resistance (R_{tot}) of the electrode. The difference between the two intercepts corresponds to polarization resistance (R_p, or area specific resistance ASR) [37]. The R_p, R_o and R_{tot} values obtained from the impedance spectra at 800 °C are displayed in the inset of Fig. 12. The results are also displayed in Table 2. The value of R_p is low; it increases from 0.07 Ω cm^2 for $x = 0.5$ to 0.156 Ω cm^2 for $x = 1.5$, indicative of high oxygen-ion transport in the interface between PBSCF cathode and LSGM electrolyte. The R_p presents the overall cathodic properties related with the oxygen reduction, oxygen surface/bulk diffusion and the gas-phase oxygen diffusion [38]. The evolution of R_p demonstrates that the electro-catalytic activity for oxygen reduction reaction decreases with increasing Fe content x. This is because the Co ions have higher electro-catalytic activity than Fe ions. The microstructure, R_p value and electronic conductivity are critical to the

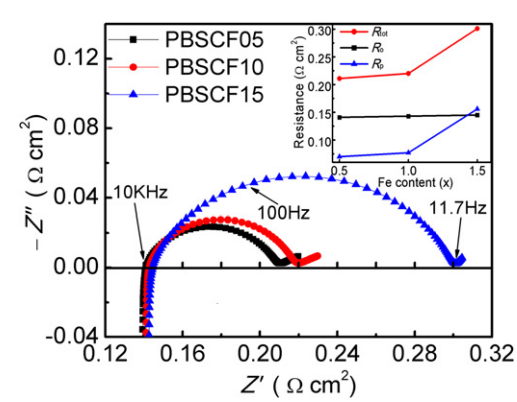

Fig. 12. Impedance spectra measured at 800 °C on symmetric PBSCF cathodes on LSGM electrolyte.

power output of the fuel cell. Why the PBSCF05 exhibits the best electrochemical performance should be ascribed to its porous microstructure, high conductivity and low electrochemical resistance.

4. Conclusions

In order to lower the TECs and optimize the electrochemical performance of the layered perovskite cathode, $PrBa_{0.5}Sr_{0.5}Co_{2-x}Fe_xO_{5+\delta}$ ($x = 0.5$, 1.0, 1.5) were systematically investigated as potential cathodes for LSGM electrolyte-supported solid oxide fuel cells. For PBSCF, the lattice constant increases and the oxide phase structure keep unchanged with increasing Fe content. All samples exhibit a semiconductor–metal transition, and the transition temperature increases as the Fe content increases. The TEC decreases from 21.3×10^{-2} K^{-1} to 19.2×10^{-6} K^{-1} with increasing Fe content from $x = 0.5$ to 1.5, which is favorable to the compatibility with the LSGM electrolyte. The polarization resistance of the PBSCF cathode increases from 0.07 Ω cm^2 at $x = 0.5$ to 0.156 Ω cm^2 at $x = 1.5$, which deteriorates the electrode performance. The maximum power density of single cell fabricated with PBSCF cathodes is 697, 649 and 456 mW cm^{-2} at 850 °C for $x = 0.5$, 1.0 and 1.5, respectively. Our experiment indicates that the PBSCF layered perovskites are promising cathode materials for SOFCs.

Acknowledgments

This work was supported by the Natural Science Foundation of China (Grants 50825203 and 21175050) and the PCSIRT (Program for Changjiang Scholars and Innovative Research Team in University, IRT1014). In addition, the authors thank the Analytical and Testing Center of Huazhong University of Science and Technology for XRD, SEM measurement.

References

[1] B.C.H. Steele, A. Heinzel, Nature 414 (2001) 345–352.
[2] Y.H. Huang, R.I. Dass, Z.L. Xing, J.B. Goodenough, Science 312 (2006) 254–257.
[3] A. Orera, P.R. Slater, Chem. Mater. 22 (2010) 675–690.
[4] V. Pralong, V. Caignaert, S. Hebert, A. Maignan, B. Raveau, Solid State Ionics 177 (2006) 1879–1881.
[5] A.J. Jacobson, Chem. Mater. 22 (2010) 660–674.
[6] K. Zhang, L. Ge, R. Ran, Z.P. Shao, S.M. Liu, Acta Mater. 56 (2008) 4876–4889.
[7] A.A. Taskin, A.N. Lavrov, Y. Ando, Appl. Phys. Lett. 86 (2005) 091910.
[8] A. Maignan, C. Martin, D. Pelloquin, N. Nguyen, B. Raveau, J. Solid State Chem. 142 (1999) 247–260.
[9] C. Frontera, A. Caneiro, A.E. Carrillo, J. Oró-Solé, J.L. García-Muñoz, Chem. Mater. 17 (2005) 5439–5445.
[10] G. Kim, S. Wang, A.J. Jacobson, L. Reimus, P. Brodersen, C.A. Mims, J. Mater. Chem. 17 (2007) 2500–2505.
[11] C.J. Zhu, X.M. Liu, C.H. Yi, D.T. Yan, W.H. Su, J. Power Sources 185 (2008) 193–196.
[12] D.J. Chen, R. Ran, K. Zhang, J. Wang, Z.P. Shao, J. Power Sources 188 (2009) 96–105.
[13] L. Zhao, B.B. He, B. Lin, H.P. Ding, S.L. Wang, Y.H. Ling, R.R. Peng, G.Y. Meng, X.Q. Liu, J. Power Sources 194 (2009) 835–837.
[14] M. Yadav, W.Q. Gong, A.J. Jacobson, J. Solid State Electrochem. 15 (2011) 293–301.
[15] H.P. Ding, X.J. Xue, Electrochim. Acta 55 (2010) 3812–3816.
[16] J.H. Kim, M. Cassidy, J.T.S. Irvine, J. Bae, J. Electrochem. Soc. 156 (2009) B682–B689.
[17] J.H. Kim, A. Manthiram, J. Electrochem. Soc. 155 (2008) B385–B390.
[18] Y.H. Huang, G. Liang, M. Croft, M. Lehtimäki, M. Karppinen, J.B. Goodenough, Chem. Mater. 21 (2009) 2319–2326.
[19] T. Wei, Q. Zhang, Y.H. Huang, J.B. Goodenough, J. Mater. Chem. 22 (2012) 225–231.
[20] Y.N. Kim, J.H. Kim, A. Manthiram, J. Power Sources 195 (2010) 6411–6419.
[21] J.L.G. Fierro, Catal. Today 8 (1990) 153–174.
[22] L.L. Zhang, Q.J. Zhou, Q. He, T.M. He, J. Power Sources 195 (2010) 6356–6366.
[23] H. Falcón, J.A. Barbero, G. Araujo, M.T. Casais, M.J. Martínez-Lope, J.A. Alonso, J.L.G. Fierro, Appl. Catal. B Environ. 53 (2004) 37–45.
[24] J. Jung, D.D. Edwards, J. Solid State Chem. 184 (2011) 2238–2243.
[25] H. Falcón, J.A. Barbero, J.A. Alonso, M.J. Martínez-Lope, J.L.G. Fierro, Chem. Mater. 14 (2002) 2325–2333.
[26] J.W. Stevenson, T.T. Armstrong, R.D. Carneim, L.R. Pederson, W.J. Weber, J. Electrochem. Soc. 143 (1996) 2722–2729.
[27] J.W. Moon, Y. Masuda, W. Seo, K. Koumoto, Mater. Sci. Eng. B 85 (2001) 70–75.
[28] L. Zhao, J.C. Shen, B.B. He, F.L. Chen, C.R. Xia, Int. J. Hydrogen Energy 36 (2011) 3658–3665.
[29] A. McKinlay, P. Connor, J.T.S. Irvine, W.Z. Zhou, J. Phys. Chem. C 111 (2007) 19120–19125.
[30] H.L. Zhao, W. Shen, Z.M. Zhu, X. Li, Z.F. Wang, J. Power Sources 182 (2008) 503–509.
[31] K. Conder, E. Pomjakushina, V. Pomjakushin, M. Stingaciu, S. Streule, A. Podlesnyak, J. Phys. Condens. Matter 17 (2005) 5813–5820.
[32] Q. Zhang, T. Wei, Y.H. Huang, J. Power Sources 198 (2012) 59–65.
[33] K.T. Lee, A. Manthiram, Solid State Ionics 176 (2005) 1521–1527.
[34] G.C. Kostogloudis, N. Vasilakos, C. Ftikos, Solid State Ionics 106 (1998) 207–218.
[35] L.W. Tai, M.M. Nasrallah, H.U. Anderson, D.M. Sparlin, S.R. Sehlin, Solid State Ionics 76 (1995) 259–271.
[36] J.H. Kim, M. Cassidy, J.T.S. Irvine, J. Bae, Chem. Mater. 22 (2010) 883–892.
[37] E.P. Murray, S.A. Barnett, Solid State Ionics 143 (2001) 265–273.
[38] S.W. Baek, J.H. Kim, J. Bae, Solid State Ionics 179 (2008) 1570–1574.